nature portfolio

https://doi.org/10.1038/s41563-021-01094-0

Supplementary information

Deterministic inverse design of Tamm plasmon thermal emitters with multi-resonant control

In the format provided by the authors and unedited

Supplementary Information

Deterministic Inverse Design of Tamm Plasmon Thermal Emitters with Multi-Resonant Control

Mingze He[1,6*], J. Ryan Nolen[2,6], Josh Nordlander[3], Angela Cleri[3], Nathaniel S. Mcllwaine[3], Yucheng Tang[4], Guanyu Lu[1], Thomas G. Folland[1, 5], Bennett A. Landman[4], Jon-Paul Maria[3], Joshua D. Caldwell[1, 4*]

1. Department of Mechanical Engineering, Vanderbilt University, Nashville, Tennessee, USA
2. Interdisciplinary Materials Science Program, Vanderbilt University, Nashville, Tennessee, USA
3. Department of Materials Science and Engineering, The Pennsylvania State University, University Park, Pennsylvania, USA
4. Department of Electrical Engineering and Computer Science, Vanderbilt University, Nashville, Tennessee, USA
5. Department of Physics and Astronomy, The University of Iowa, Iowa City, Iowa, USA
6. These authors contributed equally

* Email: mingze.he@vanderbilt.edu; josh.caldwell@vanderbilt.edu

Section 1. Highly customized error for special designs

In the main text, we mentioned that the error is written in a combination of mean-squared error (MSE, the first term) and mean absolute error (MAE, the second term) terms:

$$error = mean\left\{ratio1 \cdot \left(\overrightarrow{DS} - \overrightarrow{TS}\right)^2 + ratio2 \cdot \left|\left(\overrightarrow{DS} - \overrightarrow{TS}\right)\right|\right\} \quad \text{Eq. (1)}$$

While the MSE regulates the algorithm to focus on spectral ranges where the difference between designed (DS) and target spectra (TS) is greatest, MAE treats every frequency point as equally important. If the TS is a spectrum that can be matched perfectly, e.g., a single peak design over a narrow frequency range, the hyperparameter choice does not matter. Yet, when the design cannot be accomplished as well, e.g., matching a complicated spectrum of a chemical, if one cares more about the overall matching (such as baseline) than the peak matching, the MAE should have a larger component than MSE. Here, we use the design details in **Fig. 3c** as an example to show the technique of *weighed sampling*. Since we are optimizing the TPP-EM based on the frequency points, we can artificially make some frequency range more/less important by sampling it more densely/sparsely, and we can also artificially ignore certain frequency ranges.

For example, for free-space communications, the performance of WS-EM in the water absorption band can be ignored since the energy will be attenuated through space propagation. However, for NDIR sensing, the emission in the water absorption band is required to be minimal so that the signal will not be influenced by humidity.

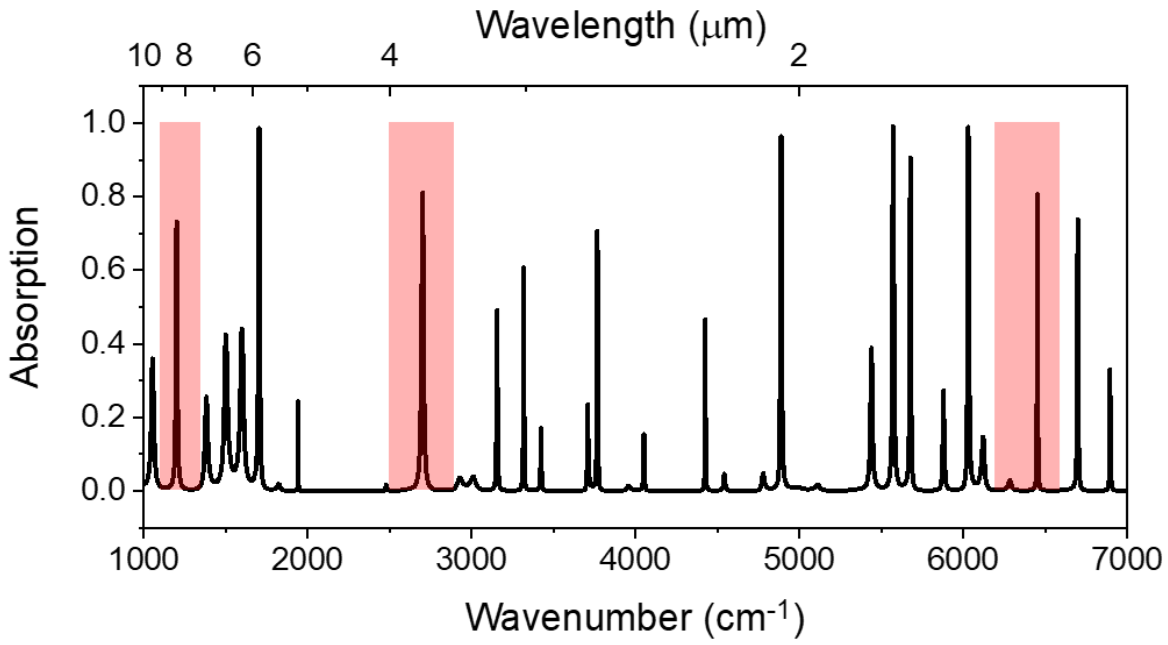

Fig. S1. Spectrum in full range, same structure in Fig. 3c. Semi-transparent boxes are the frequency ranges shown in **Fig. 3c**.

In the case presented in **Fig. 3c**, only three discrete frequency ranges are optimized: LWIR (1100-1300 cm^{-1}), MWIR (2600- 2800 cm^{-1}) and telecommunications (1.5-1.6 μm) bands, so that a single TPP-EM working over such a dramatically broad frequency range can be realized. The spectrum of this device in full range is shown in **Fig. S1.** In a commercially designed scenario, such a technique can be used to specifically optimize the frequency ranges where band-pass filters are not available or are cost-prohibitive.

Still in the case presented in **Fig. 3c**, we assume that the performance in the telecommunications band is more important than in the LWIR, so we sample the former more densely: one frequency point every 0.5 cm^{-1} in the telecommunications band, while only every 2 cm^{-1} in the LWIR and MWIR. This is of extreme importance, since trade-offs are unavoidable for a product design, and our algorithm quantifies this trade-off to "prioritize" certain ranges, as dictated by human intervention.

Section 2. The superiority of SGD in TPP-EM designs

In the optimization process, each frequency (wavelength) point is considered as an individual sample, and the absorption at that frequency is compared with the target value. Within the canonical gradient descent (GD) method, the difference across the entire data distribution is calculated and summed together to find the gradient, and all parameters are evaluated with the same computational complexity. With stochastic gradient descent (SGD), in each iteration, only a sub-sample of data points is used to find the gradient and update the vector representing the thickness and carrier concentration. The selected portion is randomly chosen from the entire collection of data points, so the algorithm is known as "stochastic" gradient descent, (SGD)[1-4]. The specific version we employed here is adaptive moment estimation (Adam) optimization[4]. Exemplary code is published on our group website[5]. In deep learning, SGD is considered to outperform GD and avoid poor local minimums[1-4], with theoretical studies proving it[1-4].

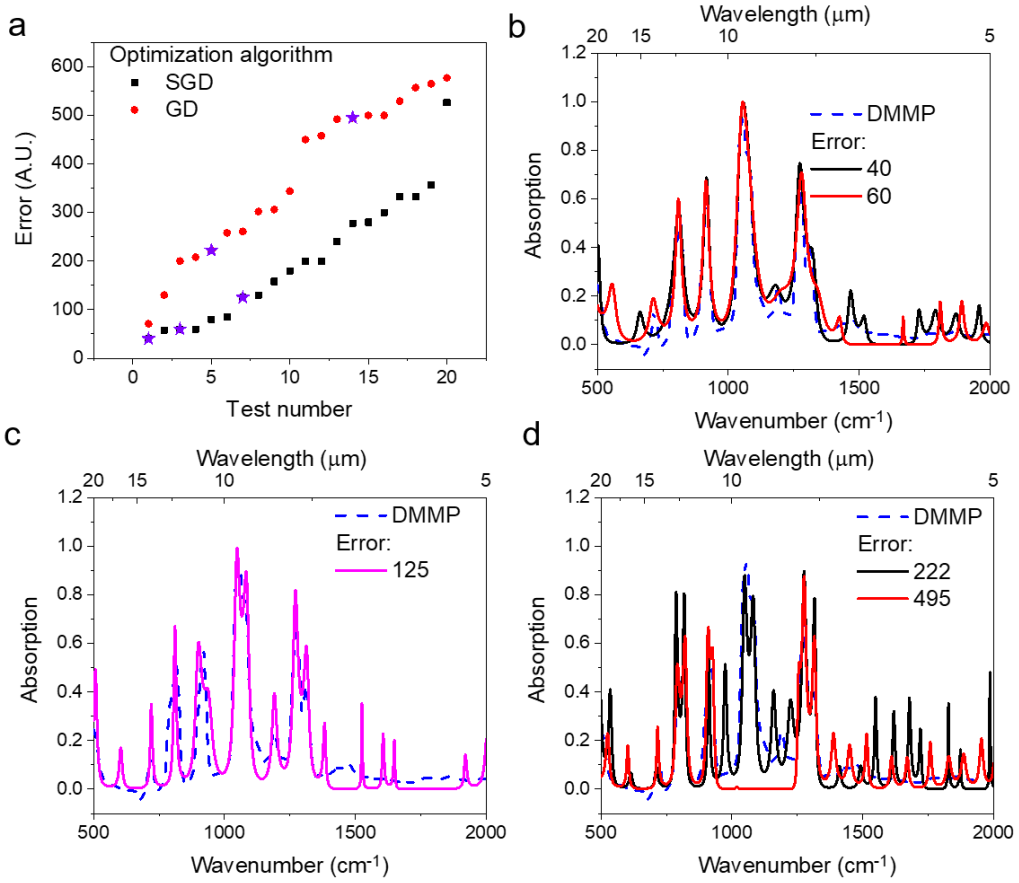

Fig. S2. The comparison of SGD and GD. (a) Error of optimized structure in 20 runs, performed with SGD and GD, respectively. Stars are the points used in panel b-d. (b-d) Designed spectra featuring different errors.

Here, to demonstrate that the SGD provides a better optimization than GD, we performed a series of optimizations on the same target: matching DMMP nerve agent and evaluating the performance based on mean-squared difference error (MSE). With SGD, the overall error is significantly lower than the

optimization performed with GD. Within 20 optimization runs, the lowest error with SGD is ~40, while this value is ~70 for GD (**Fig. S2a**). To visualize the arbitrary unit "error", we plot the designed spectra with different errors against the target spectra (**Fig. S2b-d**). While the main features are matched for errors below 100 (**Fig. S2b**), designs with higher errors lose one or several of the main absorption peaks.

Section 3. Comparison among different design strategies

To design a TPP-EM, there are several strategies proposed and applied in the literatures. Here we discuss their advantages and limitations. Our algorithm provides a well-balanced optimization performance: high efficiency and high accuracy. We would like to stress again that the code is open-sourced and can be downloaded from our group website[6] as well as Nature Materials.

Table S1. Comparison among different design strategies.

Strategy	**Global or local optimization?**	**Advantages**	**Disadvantage**	**Demonstrated designs**
Particle Swarm[7]	Global	Good global optimization	Extremely slow (hours to months)	Single-peak
Bayesian optimization[8]				Single-peak
Genetic algorithm[9]				Single-peak
Forward design [10,11](intuition and parameter sweep)	Not applicable	Clear physics understanding	Does not work for high-dimensional optimizations	Single-peak
Deep learning (neuron network)[12]	Depends on the specific network structure	Extremely quick optimization (seconds or sub-seconds)	Poor precision compared with other strategies	Single-peak
Ours	Local optimization	Efficient optimizations (minutes) High precision compared with deep learning approach	Chances to stuck at local minimums (see section 4)	Arbitrarily required spectrum

Section 4. Sample thickness and photo

The layer thicknesses of as-grown samples are characterized by cross-sectional SEM (XSEM). The designed and as-grown layer thickness are tabulated in **Table. S2**, and the carrier densities (N_a) of CdO are

also listed. One exemplary XSEM of the 7-layer sample designed to emit at three specific, disparate resonant frequencies (**Fig. 2d**) is provided in **Fig. S3.** One wafer-scale TPP-EM device is shown in **Fig. S4.**

Table S2. Layer thickness of samples. Units of thickness are in nanometers.

	3 layer Fig. (2a) LWIR emitter		3 layer (Fig. 2b) CO_2 NDIR		5 layer (Fig. 2c) CO_2+SO_2 NDIR		7 layer (Fig. 2d) Triple-peak design	
	Designed	**As-grown**	**Designed**	**As-grown**	**Designed**	**As-grown**	**Designed**	**As-grown**
Ge	Air		Air		Air		298	228
AlO_x							520	540
Ge					389	468	766	755
AlO_x					797	290	205	200
Ge	499	540	270	250	494	450	592	627
AlO_x	829	440	430	590	310	268	152	198
Ge	315	400	656	641	494	644	215	208
CdO N_d (cm^{-3})	0.7e+20		3.6e+20		3.6e+20		3.5e+20	

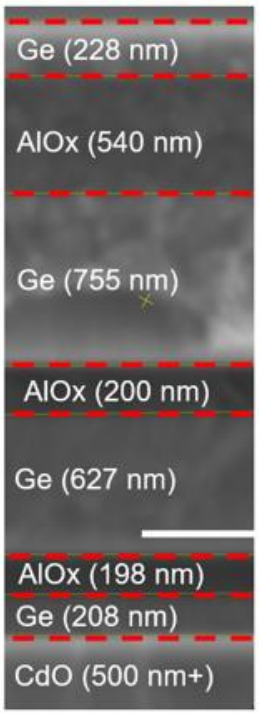

Fig. S3. XSEM image of the 7-layer sample in Fig. 2d. The scale bar is 500 nm.

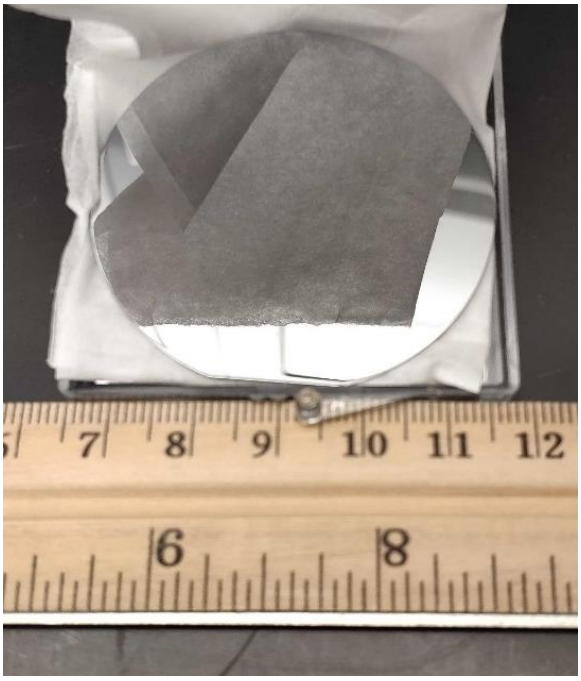

Fig. S4. A photo of our wafer-scale TPP-EM. The substrate is a 2-inch sapphire wafer.

Section 5. Dielectric function fitting of materials used: CdO, Ge and AlOx

The fitting of the dielectric function of CdO has been studied in our previous publication[13] extensively. We followed the same process to determine the dielectric function and carrier concentrations of CdO in this study. Both exemplary tabulated dielectric function and a MATLAB script to generate the dielectric function of CdO with user-defined carrier concentration from 1000 to 5000 cm^{-1} are downloadable from our group website[5]. This MATLAB script is also integrated into our inverse-design code (open-sourced and downloadable from our group website[5] and Nature Materials).

The dielectric functions of as-grown Ge and AlO_x were extracted using IR-VASE ellipsometry measurements, as shown in **Fig. S5**. The fitting was performed with WVase software from J.A. Woolam, Inc[14].

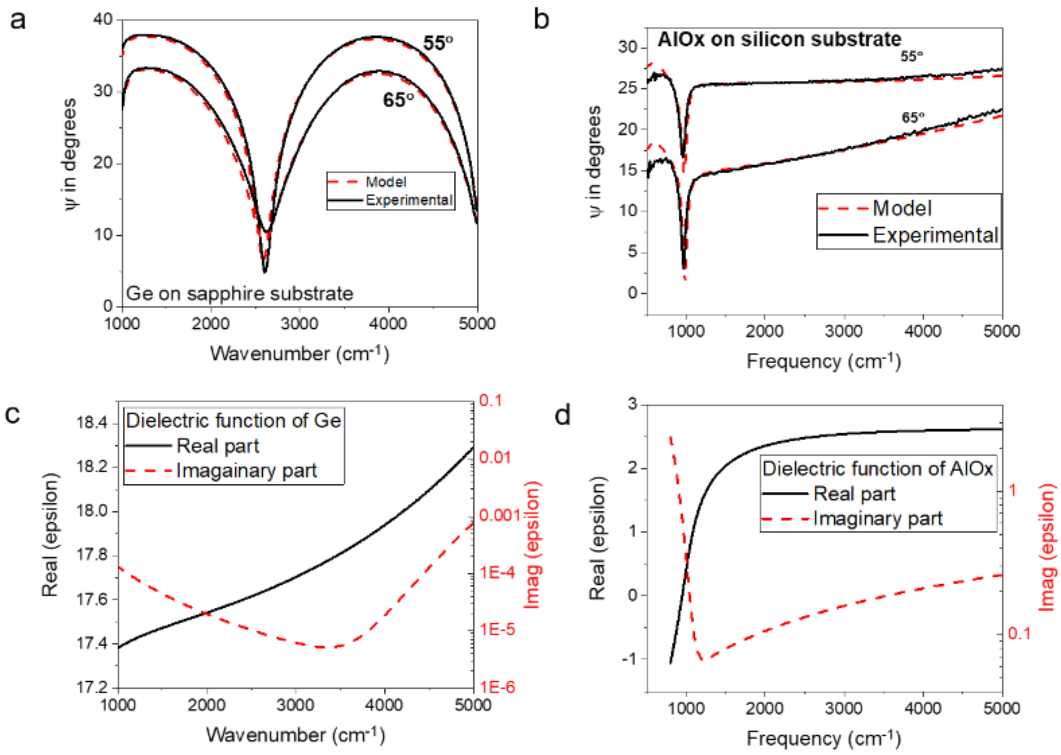

Fig. S5. Dielectric function fitting of Ge and AlO_x. Ellipsometry measurements of Ge on sapphire (a) and AlO_x on silicon (b). Fitted dielectric function of Ge (c) and AlO_x (d).

Based on the literature, we assume the thermal expansion of each of the constituents can be ignored (below 0.1%) for operating temperatures below 300 °C[15]. Based on reference[16], we assume that the dielectric function of AlOx maintains a constant over temperature. The permittivity of Ge at 150 °C is modeled based on measurements at high temperature by varying the high-frequency permittivity. We determined that at 150 °C the high-frequency permittivity is 0.5 higher than at room-temperature (**Fig. S6**), in agreement with the reference[14].

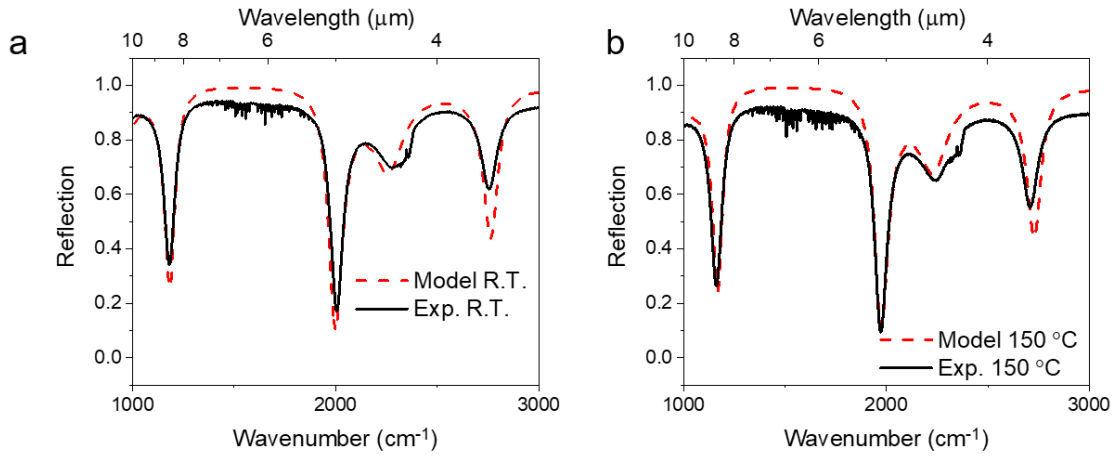

Fig. S6. Reflectance at two temperatures. (a) room temperature; (b) 150 °C

Section 6. Achievable complexity of the spectrum with different layer numbers

Here we discuss what are achievable complexity for a TPP-EM with a defined number of dielectric layers. As the complexity of the spectrum is not something that can be fully quantified and is application-specific, we employ three cases: (1) determine the achievable Q-factor at a given frequency (2350 cm^{-1} here) with 3, 5, 7, 9 and 11 dielectric stacks; (2) for the task presented in **Fig. 2d** (triple peak design) we calculate the best-matched spectrum achievable limiting to 3, 5, 7, 9 and 11 dielectric stacks; (3) to match a complicated spectrum, i.e., DMMP we repeat this process, but using 7, 11, 19, and 29 dielectric layers. In this section, the dielectric materials used are Ge and ZnSe, with permittivity values of 16+0i and 5.25+0i.

From this set of comparisons, we conclude that more complicated spectra, i.e., referring to Q-factors and number of peaks, can be achieved with increasing numbers of dielectric layers in the stack (**Fig. S7a**). Note that for a given application, i.e., multi-peak design with requested Q-factors, more dielectric stacks do not guarantee better results. For the task in **Fig. S7b**, using more than 9 dielectric layers does not provide significantly better results, even if the "error" is found to reduce, the difference in spectral match is negligible.

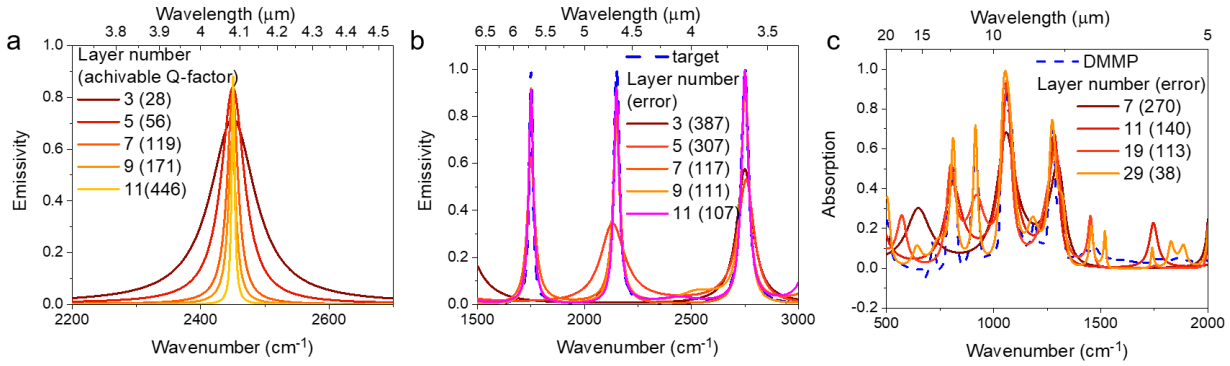

Fig. S7. Achievable complexity of spectra with different dielectric numbers. (a) highest Q factor at a given frequency (2450 cm^{-1} here); (2) triple peak design shown in Fig. 2d; (3) Matching the absorption of DMMP nerve agent.

In summary, with more layers, more complicated spectra can be matched, and if a TS can be achieved with a given number of dielectric stack layers, increasing this further does not provide significant additional advantages. For our experimentally demonstrated structures, we initiated the design by determining if the optimization is achievable with 3 dielectric layers, if yes, we use it to minimize the potential error on the

layer thickness, which are the cases for **Fig. 2a, b**. If the function is not achievable via three-dielectric-stacks, we attempt with an increasing number of layers until a suitable match is found.

Section 7. NDIR working principles

Conventional NDIR sensors consist of a gas cell containing a broadband emitter and broadband detector integrated with a narrow bandpass filter that is transmissive at the vibrational frequency of the analyte of interest (**SI, Fig. S8a**). The presence of the gas of interest within the cell results in a drop in the detected transmission, with the difference in amplitude being related to the molecular concentration in accordance with Beer's Law. Due to the simple design and small footprint, these sensors are commonly implemented in industrial settings, however, they suffer from inherent inefficiencies since off-resonant emission from the broadband emitter is not used and must be filtered. Therefore, there has been significant interest in improving the design and expanding the functionality of NDIR sensors by combining the functionality of the emitter and bandpass filter into a single device. Approaches towards filterless NDIR devices are in some iterations comprised of (1) WS-EM, (2) the gas cell, and (3) a broadband detector, such as a thermopile, as shown in **Fig. S8b**. The emission frequency of the WS-EM is normally centered at the absorption frequency of the gas of interest with a sufficiently high Q-factor so as to eliminate false-negatives that would result from non-negligible absorption from other gases that may be present. There are normally two detectors, one is shown in **Fig. S8**, and the other is to measure the power with reference gas, e.g., nitrogen, so that the power difference can be acquired.

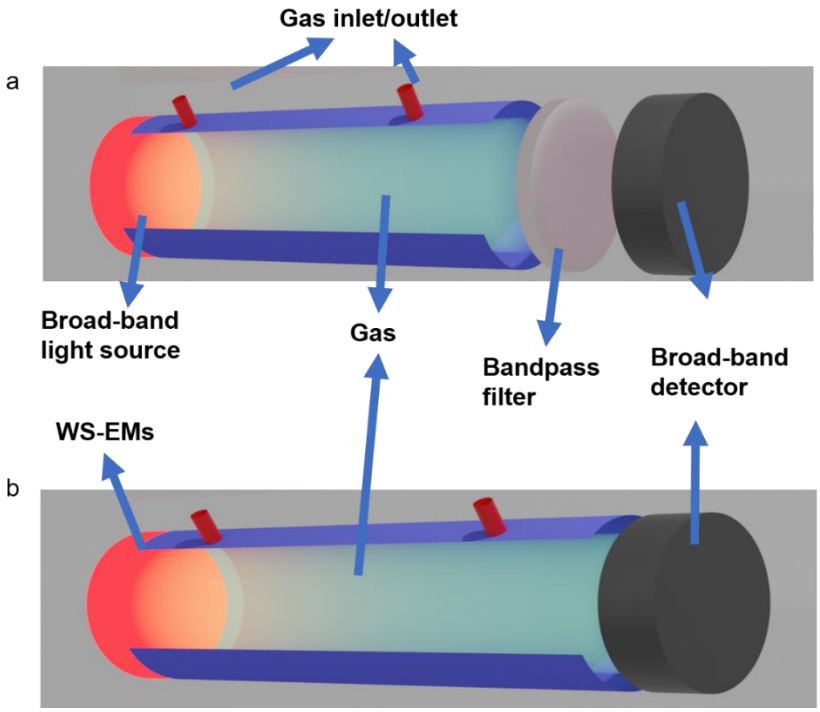

Fig. S8. Schematic of NDIR of (a) broadband light source with filter and (b) filterless NDIR enabled by WS-EM

Section 8. Rationales of target spectrum in Fig. 2c, d

In **Fig. 2c** we also demonstrated a TPP-EM for dual-gas sensing. The target is to match absorption features of SO_2 and CO_2 absorption simultaneously. In order to determine a TS to design this device, we take the absorption spectra of SO_2 and CO_2 from National Institute of Standards and Technology (NIST), then we use an envelope spectrum to cover the two main absorption peaks of SO_2 and CO_2 (**Fig. S9a**). Because numerous gases possess absorption bands in the 1000-1500 cm^{-1} spectral range, for instance CH_4, and the thermal emission leads to more energy in the lower frequency range, the target spectrum at 1380 cm^{-1} is set to be sharper (20 cm^{-1} FWHM) to reduce the energy emitted to compensate. The FWHM at 2360 cm^{-1}, which is the absorption peak of CO_2, is set to be larger (50 cm^{-1}) to compensate for the low emitted power dictated by Plancks' Law. The frequency range is set between 1000 cm^{-1} and 2500 cm^{-1}. We do not try to match below 1000 cm^{-1} as the loss of AlO_x is hard to predict, especially at elevated temperatures, however, it is important to note that emission at lower energies can be very efficiently removed via a long-pass filter. The high frequency is set to be 2500 cm^{-1} because the emitted power drops significantly above this value for the temperatures we propose to operate, as dictated by Planck's Law, and thus emission at higher frequencies can be considered negligible.

The same rationale is also used to create the target spectrum for CO and formaldehyde dual gas sensing (**Fig. S9b**). The target spectrum has increasing FWHM with increasing frequencies: 20, 30 and 40 cm^{-1} for peaks at 1750, 2150 and 2800 cm^{-1}.

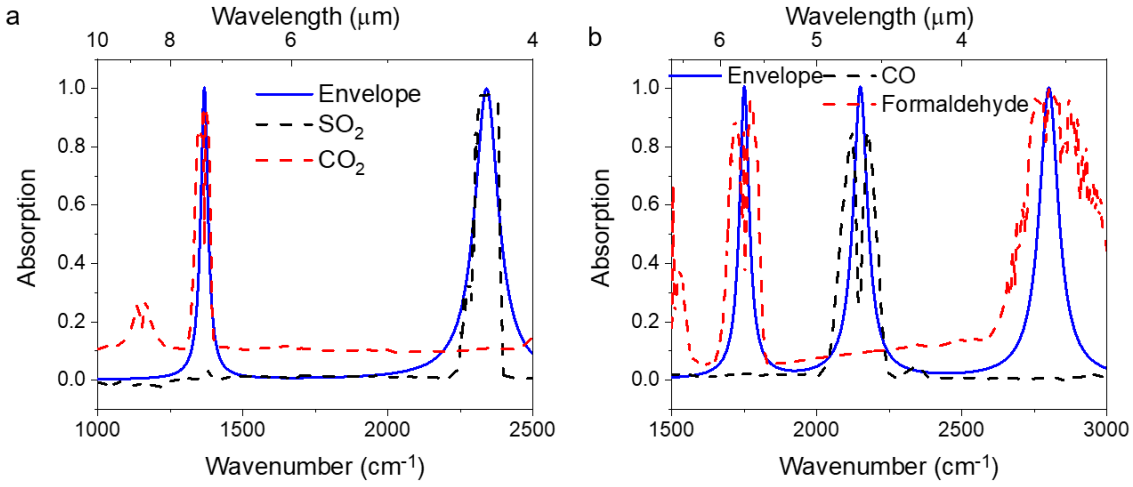

Fig. S9. Target spectrum for dual gas sensing. (a) CO_2 and SO_2; (b) CO and formaldehyde

Section 9. Differentiating CO_2 and SO_2 with a single TPP-EM by linear regression

As the emitted power is influenced by the working temperature, such a difference can be used to find the concentration of CO_2 and SO_2 by linear regression. The absorbed power of one gas, can be described as follows:

$$\overrightarrow{Emitted\ power\ of\ EM} = \overrightarrow{Emitted\ power\ of\ black\ body} \otimes \overrightarrow{Emissivity\ of\ EM} \quad \text{Eq. (2)}$$

$$\overrightarrow{Absorbed\ power} = \overrightarrow{Emitted\ power\ of\ EM} \otimes \overrightarrow{absorption\ spectrum\ of\ gas} \cdot \boldsymbol{absorption\ strength} \quad \text{Eq. (3)}$$

Where $\otimes$ stands for element-wise multiplication. The actual gas concentration in ppm can be derived from scalar $\boldsymbol{absorption\ strength}$ with the Beer-Lambert law. Assuming all the spectra are discretized from 1000 cm^{-1} to 2500 cm^{-1} into $\boldsymbol{N}$ frequency points, then each spectrum can be written as a $[\boldsymbol{N} \times \boldsymbol{1}]$ vector. Assuming we have $\boldsymbol{m}$ different temperatures, then the emitted power of the TPP-EM at $\boldsymbol{m}$ temperatures can be written in a matrix of $[\boldsymbol{N} \times \boldsymbol{m}]$, i.e., $[Emitted\ power]$, of which the rank of the matrix is $\boldsymbol{m}$, because the $\overrightarrow{Emitted\ power\ of\ black\ body}$ is linearly independent at different temperatures.

When we have multiple gas types (CO_2 and SO_2 here for example), the absorption spectra will be expanded into matrices, with different rows representing different gas types. As such, we have two unknown variables $[\boldsymbol{1} \times \boldsymbol{2}]$, i.e., $\overrightarrow{absorption\ strength}$, representing the concentrations of CO_2 and SO_2 respectively. Then the power change read by the detector is:

$$([\overrightarrow{absorption\ strength}] \times [absorption\ spectra\ of\ CO_2\ and\ SO_2]) \times [Emitted\ power\ of\ EM] = \overrightarrow{power\ change\ at\ m\ temperatures\ concentration} \quad \text{Eq. (4)}$$

where $[absorption\ spectra\ of\ CO_2\ and\ SO_2]$ is a matrix of $[\boldsymbol{2} \times \boldsymbol{N}]$ representing the absorption of CO_2 and SO_2 respectively, and $\times$ stands for matrix multiplication. In Eq. (4), $[absorption\ spectra\ of\ CO_2\ and\ SO_2]$ is pre-calibrated, [Emitted power of EM] is the measured power of WS-EM before it is assembled in the NDIR, and $\overrightarrow{power\ change\ at\ m\ temperatures\ concentration}$ is the reading from the detector. Thus, we can use a simple non-negative linear regression solution to find the vector of $\overrightarrow{absorption\ strength}$, and thus extract the gas concentrations in ppm. Non-negative linear regression can be performed by many scientific programming interfaces, such as SciPy (https://www.scipy.org/).

Example of differentiating CO_2 and SO_2 with our TPP-EM in Fig. 2c

In the case of differentiating CO_2 and SO_2 with the emitter in Fig. 2c, we can simplify the system by only considering two isolated frequency points: 1380 and 2360 cm^{-1}, as they are the only two emission peaks of our TPP-EM. As such, the emissivity vector is: [0.6 1.0]. At 100, 150, 200, 250 °C, the emitted powers ($W/m^2/sr/cm^{-1}$) of black body are:

$$\begin{bmatrix} 0.175 & 0.327 & 0.538 & 0.808 \\ 0.020 & 0.059 & 0.136 & 0.269 \end{bmatrix}$$

As such, the emitted power ($W/m^2/sr/cm^{-1}$) of our TPP-EM is:

$$\begin{bmatrix} 0.105 & 0.196 & 0.323 & 0.485 \\ 0.02 & 0.059 & 0.136 & 0.269 \end{bmatrix}$$

Assuming the concentration of SO_2 and CO_2 are leading to absorption values of **a** and **b** respectively, then the power change ($W/m^2/sr/cm^{-1}$) matrix is:

$$[0.105a + 0.02b + noise1 \quad 0.196a + 0.059b + noise2 \quad 0.323a + 0.136b + noise3 \quad 0.485a + 0.269b + noise4]$$

which are the readings of the detector at four discrete TPP-EM operating temperatures. From there, both the absorption caused by SO_2 and CO_2 can be calculated and therefore the corresponding concentrations extracted dynamically.

Why WS-EM instead of blackbody emitters?

Within the previous discussions, it appears that one could do the aforementioned calculations with any emitter type, even a blackbody, which is true when there is no noise and only CO_2 and SO_2 are present. However, other gases such as water vapor will be present in the environment, and thus, with a blackbody emitter, changes in the humidity and/or other atmospheric gases will lead to corresponding power changes, resulting in false-positives. Yet, since our TPP-EM does not emit power in the water absorption band, the selectivity will be significantly improved.

Section 10. Dielectric materials thickness error analysis

Here we discuss the influence of thickness error, i.e., how the results will be influenced when the thickness cannot be precisely controlled in experiments. In general, different combinations of layer thickness discrepancies can lead to different outcomes: (1) shifting the resonance frequency (case 2, 3); (2) broadening/sharpening the resonance linewidth (case 1, 4); (3) influencing the resonance amplitude(s) (case 1, 2, 3, 4); (4) eliminating the resonance (case 1), as shown in **Fig. S10**. Here, we vary the designed layer thickness for the device presented in **Fig. 2c** with several results provided.

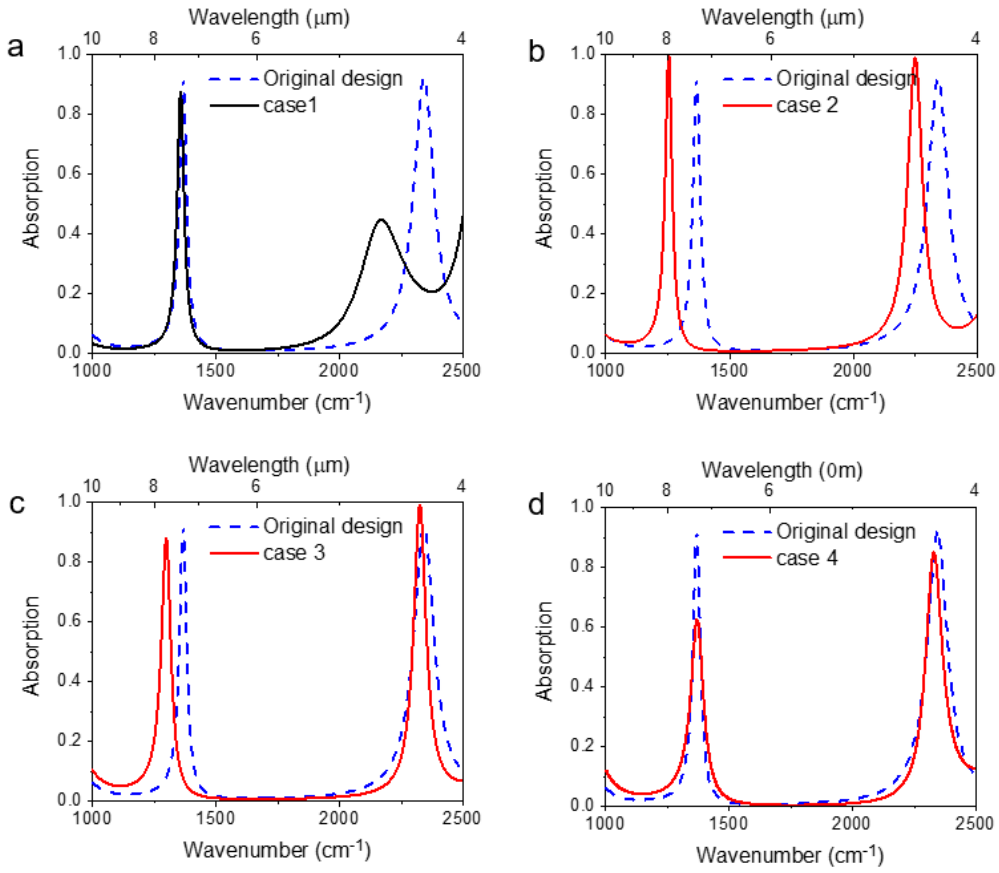

Fig. S10, Resultant spectra for structures with different thickness error.

The original design is [389 797 494 310 494] (top to bottom layer thickness, starting with Ge ending with Ge), and CdO carrier concentration is 3.6e+20 cm^{-3}. Below, bold and italic style numbers indicate that the corresponding layer thicknesses are different from the original design.

In case 1, the calculation is performed with: [***509*** 797 494 310 494]

In case 2, the calculation is performed with: [389 797 494 310 ***604***]

In case 3, the calculation is performed with: [389 ***507*** 494 310 ***604***]

In case 4, the calculation is performed with: [***468 290 450 268 644***], which is our as-grown structure.

Section 11. Peak analysis of the device in Fig. 2d

Table S3 Peak analysis of Fig. 2d

	Center (cm^{-1})	FWHM (cm^{-1})	Q	Center (cm^{-1})	FWHM (cm^{-1})	Q	Center (cm^{-1})	FWHM (cm^{-1})	Q

TS	1750	20	87.5	2150	30	71.7	2800	40	70
DS	1750.3	37.5	46.7	2152.6	32.5	66.2	2802.0	35.8	78.3
Exp.	1761.9	41	42.7	2146.7	38	56.5	2721.6	21	129.6
As-grown	1745.6	41	42.8	2134.1	30	70.4	2703.4	23	119.6

Note that the Q-factors of those peaks are ~100, which is on par with the best-reported values for isolated nanophotonic resonators using lower loss surface phonon polariton resonators (~100-400)[17-21] and plasmonic Fano structures (~100-400)[22]. The allowed Q-factors of TPP-EMs are related to the number of dielectric layers employed (**SI, section 6**).

Section 12. Evaluating the theoretical detection limitation in NDIR scheme

In an NDIR device, the power emitted from the EM will propagate through the gas cell and arrive at the detector. When the gas cell is filled with reference gas, e.g., nitrogen, the power reading on the detector is:

$$reference\ signal = emissivity\ of\ EM \times blackbody\ emission \times area\ of\ EM \times solid\ angle \quad \text{Eq. (5)}$$

Whilst in general the performance and power of the sensor is highly dependent on collection optics, we can make some approximations based on the geometry of a commercial sensor. Here, we assume the EM is a circle of 2-cm diameter, and the detector is also 2-cm diameter. The optical path length of gas cell is 10 cm, which is a typical design[23], leading to a solid angle of 2.2×10^{-4} sr. The gas absorption is determined by Beer-Lambert Law:

$$Transmission\ with\ CO_2 = \exp(-kcL) \quad \text{Eq. (6)}$$

where k is the absorption coefficient, c is gas concentration and L is the sample optical path length. From references[24-26] and NIST, we acquire or estimate the absorption spectra of CO_2, CO, SO_2 and formaldehyde at a given concentration and in a certain length of the gas cell. Thus, we are able to calculate the transmission (and equivalently, the absorption) for any concentration of CO_2. The reference power, e.g., power received by the detector when the gas cell is filled with nitrogen, can be calculated by Eq. (6). Knowing the reference power and the CO_2 transmission for a given concentration, the power collected at the detector when CO_2 is present is:

$$Detected\ power\ with\ chemical = reference\ signal \times Transmission\ with\ CO_2 \quad \text{Eq. (7)}$$

In order to determine the detection limit of a hypothetical, filterless NDIR device equipped with one of our TPP-EMs, we assume a commercial coin-sized pyroelectric detector[27] with a responsivity of 150,000 V/W, and estimated noise of 180 μV at 10 hz . For the device in Fig. 2b, we first set the working temperature as

600 °C, which is a typical design set up. At such a working temperature, when the difference between $reference\ signal$ and $Detected\ power\ with\ chemical$ is 3 σ (a signal to noise ratio of 3:1), i.e., the voltage difference is 540 μV, the CO_2 concentration is 0.5 ppm. Thus, the detection limit is determined to be 0.5 ppm. We then repeated this calculation for the device in Fig. 2c, resulting in a CO_2 (SO_2) concentration detection limit of 0.5 (3.3) ppm. For comparison, we also performed this calculation for a conventional NDIR design, i.e. assuming the same detector and gas cell, however, using a blackbody emitter at the same size coupled with a bandpass filter designed for CO_2 gas sensing[28]. Here, the resultant CO_2 concentration detection limit is also 0.5 ppm. For comparison, a commercial CO_2 NDIR detector has a detection limit of 8 ppm[29]. Despite the imperfect DBR growth technique, our TPP-EMs enabled a filterless NDIR sensor that still has identical performance for single gas sensing to a conventional blackbody/filter design, while permitting multi-gas sensing.

Building on the same assumptions, we evaluated the performance of the triple-peak design and discussed how we could benefit from such a multi-peak emitter. One obvious point we have discussed is the ability to sense multiple gases simultaneously. The other advantage is the improved sensitivity, i.e., reduced the detection limit. The detection limit of formaldehyde is 1.4 ppm with device in Fig. 2d. However, for a black body emitter with a with a bandpass filter centered at 2750 cm^{-1} with a Q-factor of 90, the detection limit is 3.1 ppm.

We also estimate the power consumption of those light sources based on the emitted power. The power consumption of NDIR light source originates from heat conduction, heat convection and emitted power (emissivity multiplied by black body emission). While conduction and convection can be reduced by using thermally isolating materials and vacuumizing the emitter environment, the emitted power is fundamentally dictated by the emissivity and temperature. Thus, we estimate the lowest possible power consumption based on the emitted power, and the value of a blackbody at 600 °C is 1.03 W, however, the power consumption of our WS-TPP-EM is only ~0.1 W. The comparison is summarized in **Table S4**.

In summary, the multi-peak design provides several advantages over conventional NDIR with single-band filters: (1) Permitted multi-gas sensing; (2) Improved sensitivity when multiple absorption bands of one chemical are matched; and (3) Reduced power consumption. While single-peak TPP-EM provides nearly identical sensitivity as conventional NDIR, the power consumption and potentially design complexity would be reduced significantly. Notably, with the current commercial filters, dual- and multi- peak designs cannot be achieved with a single filter (**Table S5**).

Table S4. Theoretical performance of NDIR with different light sources and/or filters

	Detection limit (ppm)	Emitted energy (W)	Gas types
Exp. Device Fig. 2b	0.5	0.18	CO_2
Exp. Device Fig. 2c (**Dual gas sensing**)	0.5	0.22	CO_2
	3.3		SO_2
Commercial bandpass filter (Q=40) with blackbody emitter	0.5	1.30	CO_2
Commercial bandpass filter (Q=90) with blackbody emitter	3.1	1.30	formaldehyde
Exp. Device Fig. 2d	3.2	0.16	CO
	1.4		formaldehyde
Exp. Device Fig. 2d artificially removing 1750 cm^{-1} peak	3.2	0.13	CO
	3.3		formaldehyde

Table S5. Comparison between our TPP-EMs and commercial bandpass filters. CO_2 bandpass filters are listed separately.

Source	**Center frequencies (cm-1)**	**Q-factors**	**Transmission Or Emissivity (%)**	**Multi/single band**
A[28]	1600-5000	~20-50	70-80	Single
	2340 (CO_2)	40.6	75	Single
B[29]	2000-3700	~25	65-80	Single
	2340 (CO_2)	35.5	70	Single
C[29]	1000-7000	~20-90	70-80	Single
	2340 (CO_2)	47	85	Single
D[27]	2000-4000	~20-40	70-80	Single

	2340 (CO_2)	35.5	75	Single
Our experimental demonstrations	2340 (CO_2)	20	100	Single
	2340 (CO_2)	26	100	Dual-band
	1363 (SO_2)	50	100	
	1750 (formaldehyde)	40	90	Triple-band
	2150 (CO)	60	90	
	2750 (formaldehyde)	90	65	

While we cannot experimentally perform the gas sensing measurements using our multiband emitter because CO, SO_2 and formaldehyde are all highly toxic gases, we validated that our single-peak TPP-EM provides nearly identical sensitivity as a conventional NDIR approach using a traditional blackbody emitter. For this benchmark experiment we first experimentally measured the NDIR response as a function of CO_2 concentration using a blackbody emitter (here vertically aligned carbon nanotubes, $\epsilon \sim 0.97$) and a commercial CO_2 filter (4.26 um center wavelength, 105 nm bandpass), as shown in **Fig. S11a**. We employ a broadband pyroelectric detector with a chopper wheel at 10 Hz (RM9 with Chopper). The gas cell was first purged with dry nitrogen gas, and then it was purged with 5% and 1% CO_2, respectively. Before and after the gas cell is filled with a certain concentration of CO_2 it is purged with dry nitrogen. We repeated this measurement using our TPP-EM device presented in **Fig. 2b** and then again using the device in **Fig. 2c**. The results are tabulated in **Fig. S11b**. We find that our TPP-EMs lead to larger power variations than the combination of the CO_2 filter (Q=42) and blackbody emitter, which comes from the wider linewidth of our TPP-EM peaks (Q=20 and 36) and the near-unity emissivity at the resonance frequency. Thus, our proposed TPP-EM performs similarly to a blackbody emitter combined with narrow-bandpass filter when only one absorption peak of a type gas is matched. When more bands are integrated, the additional emitting frequencies can be used to either permit multi-gas sensing (device in **Fig. 2c**) or enhanced sensitivity (device in **Fig. 2d**) by matching the absorption of multiple vibrational or rotational modes of the molecule of interest. Unfortunately, we are not able to demonstrate this concept experimentally as the gases our multiple TPP-EM emission is designed for are extremely toxic.

a

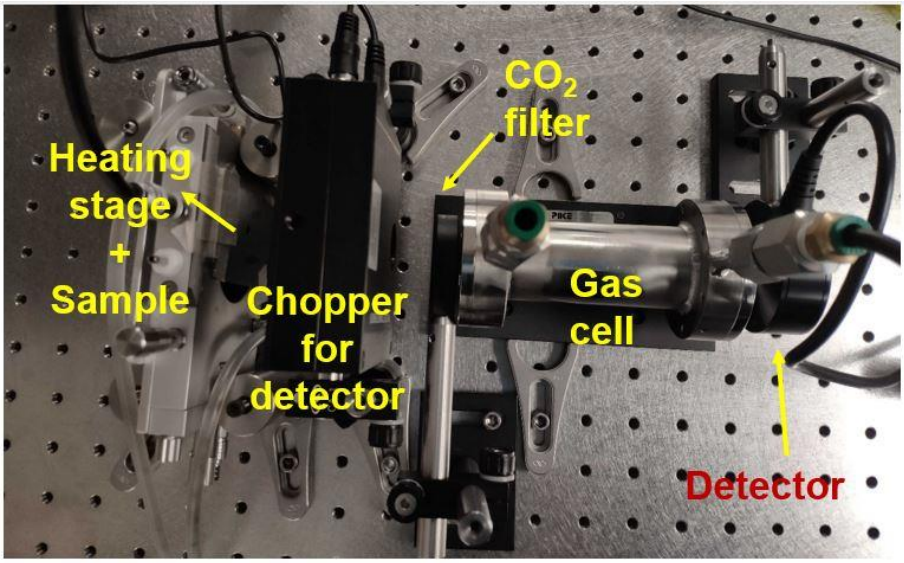

b

Power (background removed)	N_2 (μW)	CO_2 (5%) (μW)	Power change (μW)	CO_2 (1%) (μW)	Power change (μW)
Blackbody emitter + filter	0.5 (0.12)	0.12 (0.11)	**0.38 (0.16)**	0.24 (0.11)	**0.26 (0.16)**
TPP-EM (Fig. 2b)	5.3 (0.13)	4.2 (0.13)	**1.1 (0.18)**	4.9 (0.15)	**0.4 (0.20)**
TPP-EM (Fig. 2c)	5.4 (0.12)	4.18 (0.18)	**1.22 (0.21)**	4.76 (0.12)	**0.64 (0.17)**

Fig. S11, Benchmark measurements to compare our TPP-EMs with commercial technologies. (a) experimental setup and sample temperatures are 250 °C for all cases; (b)Tabulated power under different conditions, with background power removed. Standard deviations (propagated uncertainties) are included in the parentheses. The standard deviations are calculated by analyzing the detector reading over 10 seconds.

Section 13. Thermal emission measurements at different angles

As discussed in references [30,31], the angular spread of TPP-EM is limited to a small range, and TM polarized light is typically slightly more dispersive than TE polarized. Here we show the emissivity of samples in **Fig. 2c, d** at different angles and polarizations, as shown in **Fig. S12**.

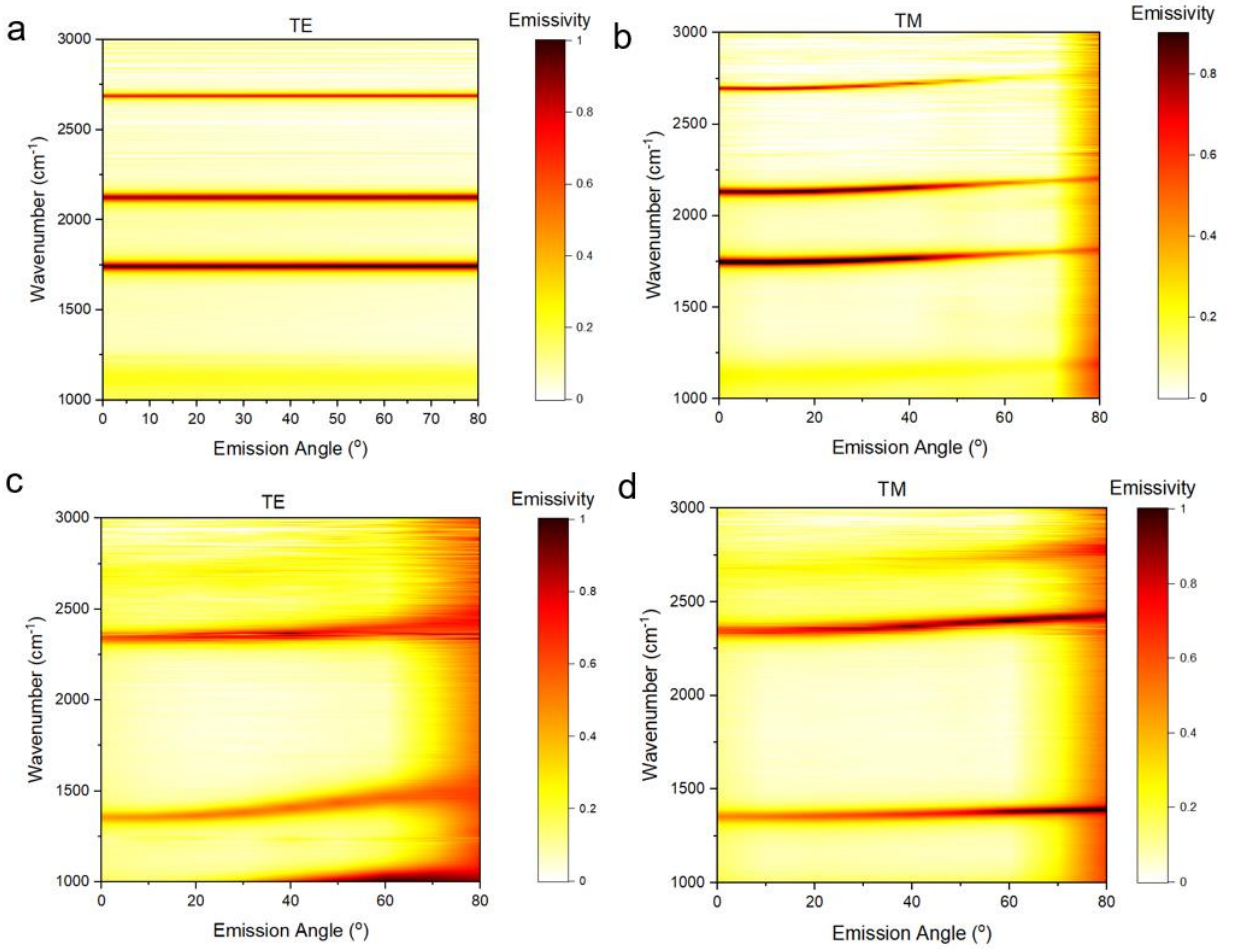

Fig. S12, Emissivity measured for two samples at different incident angles. (a-b) sample in Fig. 2d; (c-d) sample in Fig. 2c

Section 14. Designed structures in main text "Potential for inversely designed TPP-EMs"

Here, we provide the parameters of the designed structures in **Fig. 3, Fig. 4 and SI**. All of our designs consisted of a 29-layer DBR on top of a CdO bilayer with Ge as the first and last layers in the DBR. The CdO carrier concentration is constrained between 0.2 and 12.0 e+20 cm^{-3}, which is the range that has been demonstrated in literature[13,32]. A model published by our groups is used to calculate the dielectric function of CdO[13] as a function of carrier density, and the corresponding MATLAB code is published on our group website[5]. The dielectric function of Ge[33] and ZnSe[34] are considered as constants over the entire frequency range: 16+ 0i and 5.0625 +0i, respectively. The substrate is fixed to CdO with the carrier concentration of

$12.0x10^{20}$ cm^{-3} (plasma frequency=7800 cm^{-1}), so that we ensure there is no transmission. The units are all in nanometers.

Hyper-high-Q in **Fig. 3a**:

[705 681 543 854 787 872 1073 1415 1491 1120 1133 1902 1702
2396 2563 2146 2051 2066 2447 2630 2141 1979 2351 2430 1945 2291
2308 2460 1920 2500 ($\boldsymbol{N_d}$ =1.02×10^{20} cm^{-3})]

Multi-peak in **Fig. 3b**:

[4 586 689 1 622 167 166 355 195 228 214 301 184
310 259 251 202 370 270 213 196 540 561 501 343 683
698 697 177 1213 ($\boldsymbol{N_d}$ =1.86×10^{20} cm^{-3})]

LWIR to telecommunication in **Fig. 3c**:

[476 345 258 261 455 399 297 176 458 447 355 407 286
467 433 332 447 316 286 360 395 250 283 290 366
326 454 307 437 324 ($\boldsymbol{N_d}$ =6.3×10^{20} cm^{-3})]

Emissivity matching NO in **Fig. 3d**:

[64 1401 588 169 278 1047 543 636 676 736 260 619 681
448 1050 374 752 695 768 742 698 977 330 1286 922
1116 831 557 93 565 564 ($\boldsymbol{N_d}$ =0.23×10^{20} cm^{-3})]

Matching DMMP nerve agent in **Fig. 4a** with CdO:

[19 1385 270 411 770 351 603 111 553 759 583 206 480
213 876 457 1095 289 459 754 224 359 722 491 200
1009 898 1364 140 1713 ($\boldsymbol{N_d}$ =0.29×10^{20} cm^{-3})]

Matching DMMP nerve agent in **Fig. 4a** with gold (substrate is gold):

[244 394 402 314 300 421 359 404 324 284 434 591 495
374 250 396 334 454 293 275 444 369 347 474 437
491 106 442 574]

Matching CO in **Fig. S16a**:

[532 369 481 416 429 403 492 354 481 456 488 426 436
343 464 365 509 342 451 399 516 453 461 362 301
502 710 540 150 631 ($\boldsymbol{N_d}$ =0.9×10^{20} cm^{-3})]

Matching O_3 envelope in **Fig. S16b**:

[120 585 646 433 167 229 228 379 436 410 427 490 439
441 362 445 465 528 245 343 371 174 267 676 582
511 365 147 213 1313 ($\boldsymbol{N_d}$ =1.4×10^{20} cm^{-3})]

Matching CH_4 envelope in **Fig. S16c**:

[379 287 418 720 310 514 611 312 375 443 522 443 372
394 590 236 408 432 245 278 454 467 460 649 196
141 357 497 415 1116 ($\boldsymbol{N_d}$ =2.1×10^{20} cm^{-3})]

Matching NH_3 envelope in **Fig. S16d**:

[47 698 472 96 440 640 235 301 482 301 349 400 380
274 421 381 323 365 399 254 439 174 567 739 626
578 100 384 401 1582 ($\boldsymbol{N_d}$ =0.48×10^{20} cm^{-3})]

Emitted power matching N_2O in **Fig. S17**:

[92 460 759 414 98 275 726 355 174 416 305 209 191
397 63 90 200 97 144 191 148 484 440 442 363
507 358 450 134 40 ($\boldsymbol{N_d}$ =3.19×10^{20} cm^{-3})]

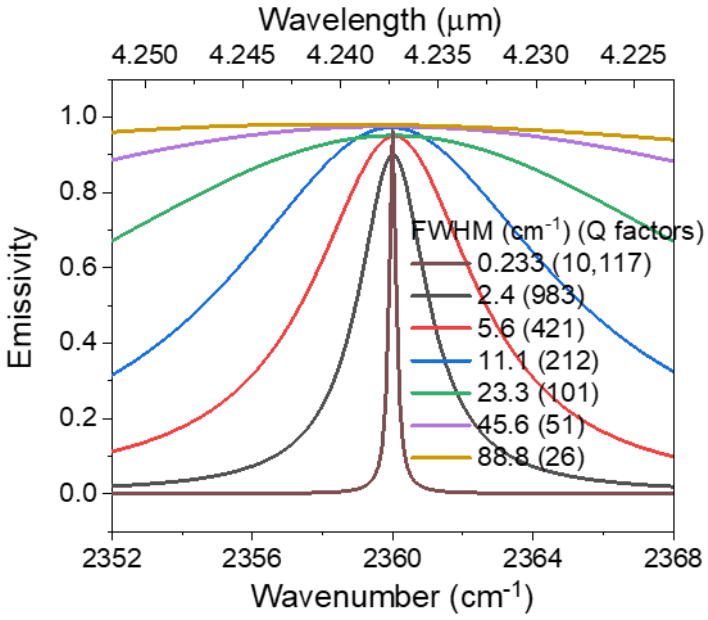

Fig. S13. The same figure in Fig. 3a, yet with much smaller frequency range to show the near-unity emissivity.

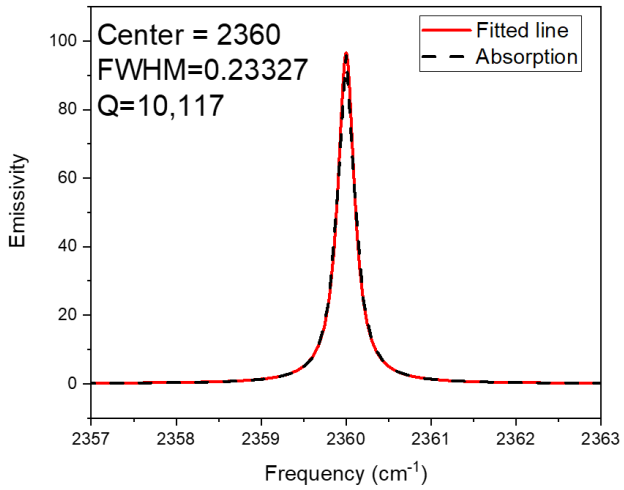

Fig. S14. The linewidth of the highest Q-factor spectra. Fitting was performed with OriginLab software with Lorentz fitting. Center and FWHM are given by the software.

Section 15. Optimized TPP-EM within different frequency ranges

Here we discuss how the "optimizing frequency range" will influence the outcomes. With a wider frequency range to optimize, the design will be more challenging due to the multi-mode nature of DBR (**Fig. S1**). Here we exemplify one case: a design for the same task presented in **Fig. 2d**, with 11 dielectric layers, with different frequency ranges integrated for the optimization routine. The three peaks remain the same, and we aim to maintain the absorption (emissivity) as zero outside of those three main peaks. From **Fig. S15 a-d**, the optimizing frequency range is progressively increased. Although our algorithm is able to suppress the side peaks well, it comes at the price of sacrificed performance for the main peaks. One can optimize the specific frequency range of interest depends on applications. For instance, in free-space communications, the performance of WS-EM in the water absorption band can be ignored since the energy will be attenuated through space propagation. One can also sample the frequency points more densely to force the algorithm to focus on that frequency of interest (**SI, section 1**), and a similar balance can also be achieved via weighted error function.

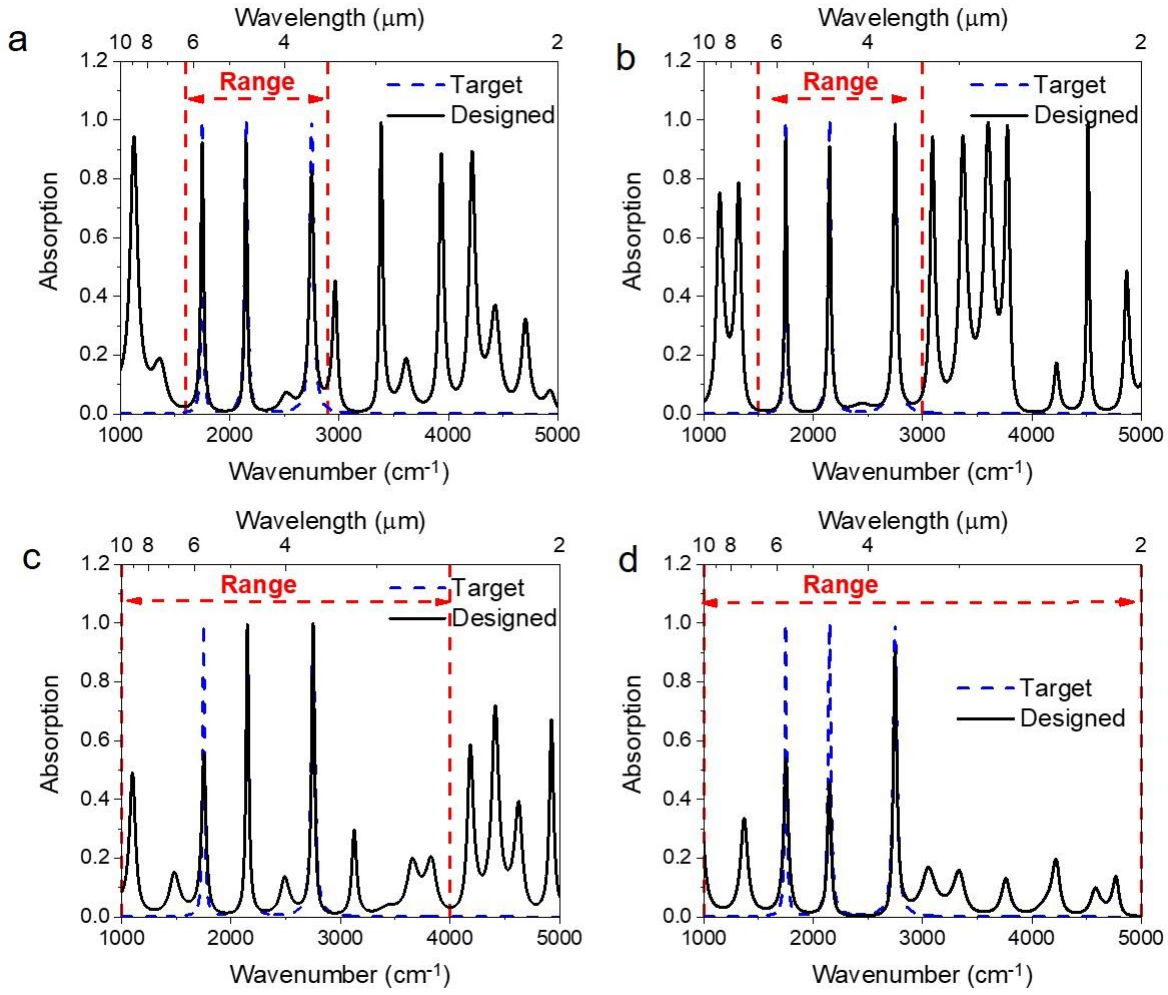

Fig. S15, Optimized TPP-EM for triple-peak design with the target frequency range varied: (a) 1600-2900 cm^{-1}; (b) 1500-3000 cm^{-1}; (c) 1000-4000 cm^{-1}; (a) 1000-5000 cm^{-1};

Section 16. More demonstrations of inversely designed TPP-EMs

We have demonstrated a number of additional TPP-EM designs, such as those matching the infrared-active vibrational spectra of nitric oxide (NO) and the nerve agent simulant dimethyl methyl phosphonate (DMMP) in the main text. Here, additional examples are provided in **Fig. S16**. Note that since the absorption spectra of O_3, CH_4 and NH_3 feature slopes or numerous sharp peaks, exact matching to the spectra cannot be realized. Instead, we use envelope spectra to cover those chemical spectra, and then employ these envelope spectra as the target spectrum (TS). All the chemical absorption spectra are from the National Institute of Standards and Technology (NIST) website.

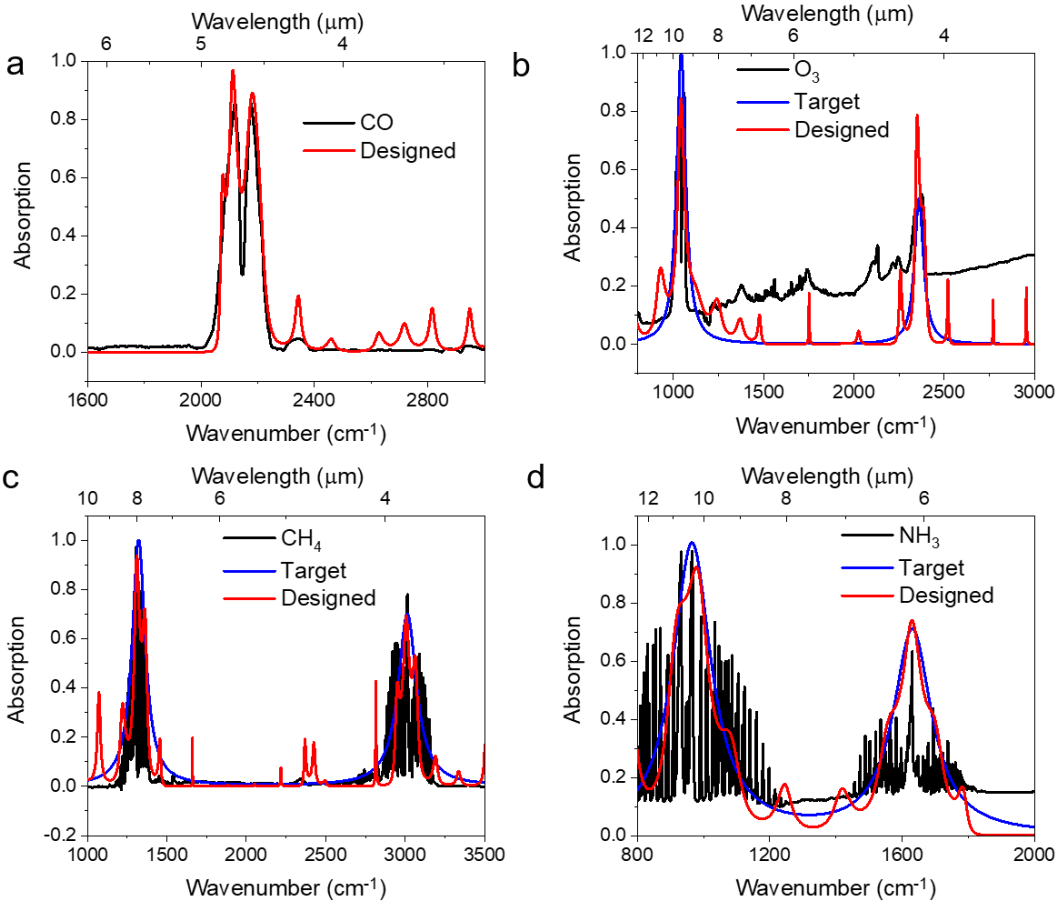

Fig. S16. More demonstrations of ID-TPP-EMs. (a) Matching CO. (b-d) Matching the envelope spectra of O_3, CH_4, and NH_4, respectively. All the chemical absorption spectra are from NIST website.

Section 17. Emitted power matching N_2O absorption spectrum

Since the emitted power is determined both by the emissivity and the temperature of the object, we designed a TPP-EM working at 250 °C to be employed for N_2O NDIR sensing. First, we determine the working temperature to be 250 °C, and this number can be adjusted according to the commercial product design based on signal strength and power consumption. Then the target emissivity spectrum becomes:

$$Target\ emissivity = normalize\ (\frac{N_2O\ absorption\ spectra}{black\ body\ emission\ at\ 250\ ^\circ C}) \qquad \text{Eq. (8)}$$

Here, the normalization is performed to make sure the highest emissivity is unity. We also remove the background absorption of N_2O.

As such, the emissivity is adjusted to the specific working temperature, as shown in **Fig. S17**.

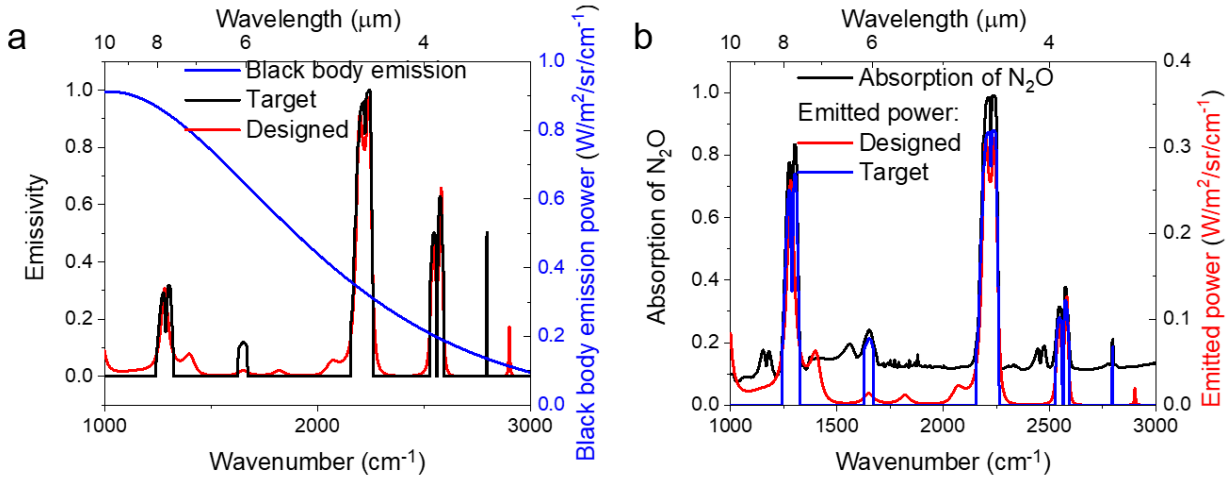

Fig. S17 Adjust the target to a specific working temperature. (a) Target emissivity and blackbody emission power spectrum; (b) target and designed emitter power.

Section 18. TPP-EM optimizations with Gold and CdO

We also performed the SGD-based inverse design using the same constraints on the total number of dielectric layers (29 layers) for both CdO and gold as the bottom conductive layer. Both optimizations were performed 20 times to ensure that a local minimum is not reported. The errors are shown in **Fig. S18**, with the structures exhibiting the lowest error values reported in **Fig. 4a**.

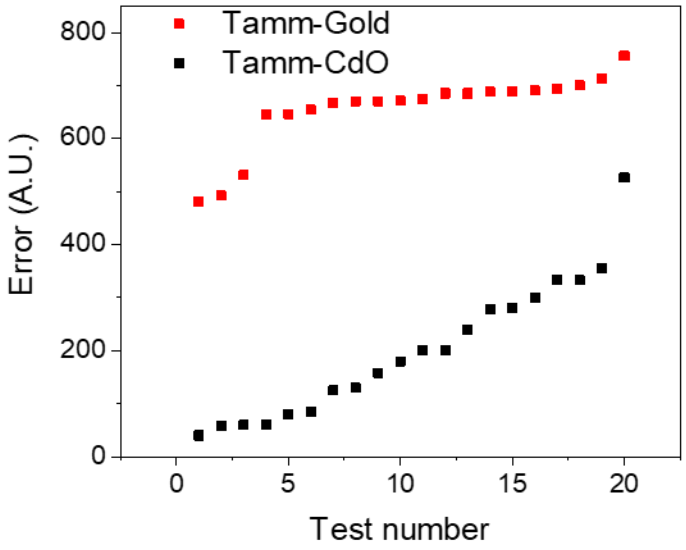

Fig. S18. The comparison between Gold and CdO supported Tamm.

Section 19. Mechanism of TPP-EM

Generally speaking, the absorption resonances supported in the TPP-EM structures fall into two categories: a Tamm-mode (cavity mode between DBR mirror and conductive substrate) and non-Tamm-mode (light transmitted from DBR being absorbed by the conductor). For a TPP mode existing within the photonic bandgap of the DBR, the reflection phase of the two mirrors (along opposing directions) must be equivalent but differ in sign ($\varphi_1 + \varphi_2 = 0$). In our work, we utilized the metal-on-bottom DBR-metal geometry where alternating layers of AlO_x and Ge are grown on top of a doped CdO film. Since TPP modes are supported at the phase-matched condition between the conductor and the DBR, one can determine whether a TPP mode will be supported at the conductor-DBR interface by calculating the Fresnel reflection coefficients directed towards the DBR and the conductor (**Fig. S19c**). There are several techniques for calculating the reflection coefficients of a multilayer structure, such as the TMM, which we use in our inverse-design calculations. However, for this simple model, we will rely on an impedance model as this method is conceptually intuitive due to its connection to circuit theory. Further, through the lumped-element model approach, this analysis can be extended to TPP-supporting films featuring a metasurface in place of the unstructured conductive film as well.

The characteristic *p*-polarized wave impedance in a material with a complex dielectric function ε_n is given as

$$Z_n = \frac{k_{z,n}}{\omega \varepsilon_o \varepsilon_n} \qquad \text{Eq. (9)}$$

where $k_{z,n} = \sqrt{k_o^2 \varepsilon_n - k_x^2}$ is the propagation constant along the z-direction, ω is the frequency, and ε_o is the permittivity of free space. From Eq. (9) it is evident that utilizing a doped semiconductor as opposed to noble metals for the conductor layer results in additional design flexibility due to the tunability of the optical impedance. Noble metals possess a large, defined carrier density and therefore the dielectric functions of these materials are also fixed. Alternatively, the plasma frequency of n-doped CdO is widely tunable throughout the IR granting additional flexibility to the design of TPP-supporting films by controlling the frequency at which the matching condition is realized for a fixed DBR stack.

With the calculated characteristic impedances of each material, we can now calculate the total lumped impedances of the DBR and conductive films. **Fig. S19c** shows the equivalent circuit model representation of a TPP film in the conductor-on-bottom geometry. To calculate the lumped impedance of the DBR, starting at the dielectric layer furthest away from the CdO-DBR interface the impedance of each layer can be calculated using a recursive method. The impedance of an individual layer with a finite thickness is given as

$$Z_{n,n+1} = Z_n \frac{Z_{n+1} + iZ_n \tan(k_{z,n} d_n)}{Z_n + iZ_{n+1} \tan(k_{z,n} d_n)} \qquad \text{Eq. (10)}$$

where d_n is the layer thickness and n is an index denoting the layer number in the stack. Z_{n+1} is the total impedance behind the layer, so when calculating the impedance of the first layer of the DBR in the CdO-on-bottom geometry $Z_{n+1} = Z_{air}$. The total impedance of the DBR (Z_{DBR}) is then solved by progressing through the remaining layers in the stack. The impedance of the CdO layer (Z_{CdO}) is calculated using the same method, however, this is thus only limited to a single layer.

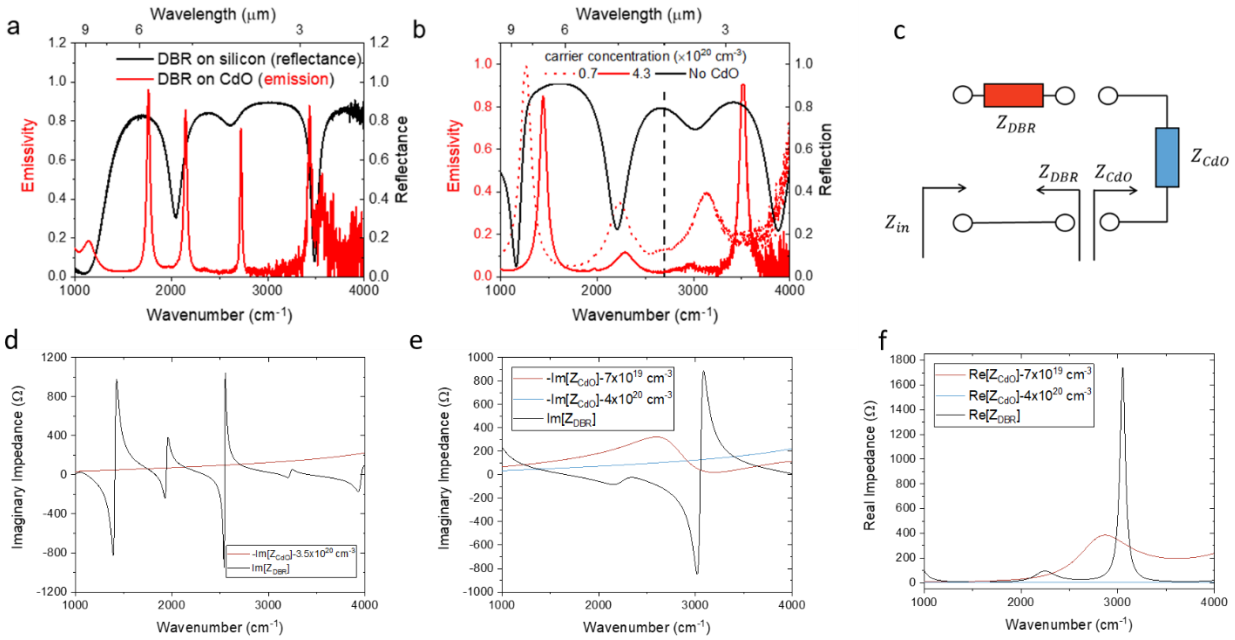

Fig. S19. Mechanism of aperiodic TPP-EM. (a) Reflectance of DBR on silicon and the emissivity of the same DBR on CdO ($N_d = 3.5x10^{20}\ cm^{-3}$). Identical film to Fig. 2d of manuscript. (b) Reflectance of DBR on sapphire and the emissivity of TPP-EMs with the same DBR but different carrier densities of CdO ($N_d = 7x10^{19}\ cm^{-3}$- dashed red line, $N_d = 4.3x10^{20}\ cm^{-3}$- solid red line). The vertical, dashed black line displays the plasma frequency of the $N_d = 7x10^{19}\ cm^{-3}$ CdO film. c) Equivalent circuit model representation of the TPP-EM film in the metal-on-bottom geometry. d) Imaginary impedance of DBR ($Im[Z_{DBR}]$, black line) and CdO ($-Im[Z_{CdO}]$, red line) from the TPP-EM in a). e) and f) Imaginary and real impedances, respectively, of DBR (black line) and two carrier densities of CdO ($N_d = 7x10^{19}\ cm^{-3}$- red line, $N_d = 4.3x10^{20}\ cm^{-3}$- blue line) from the TPP-EMs in b).

With the calculated lumped impedances Z_{DBR} and Z_{CdO} seen from the DBR-CdO interface looking in opposing directions (See arrows in **Fig. S19c**) we can now model the TP films as a simple AC equivalent circuit (**Fig. S19c**) with source and load impedances. From circuit theory, the maximum active power is dissipated by the load at the conjugate impedance-matched condition $Z_{DBR} + Z_{CdO}^{*} = 0$. In TPP films, this translates to a TPP mode being supported when $Im[Z_{DBR}] = -Im[Z_{CdO}]$, and the absorption maximized when $Re[Z_{DBR}] = Re[Z_{CdO}]$ as well.

To illustrate this further, we provide the reflectance (black line) of an aperiodic DBR (on Si) and the emission (red line) from a TPP-EM (on CdO, $N_d = 3.5x10^{20}\ cm^{-3}$) with an identical DBR in **Fig. S19a**. In **Fig. S19d** we provide the imaginary part of the DBR ($Im[Z_{DBR}]$) and the CdO layer ($-Im[Z_{CdO}]$) impedances for this TPP-EM. From **Fig. S19a, d**,, the peaks in emissivity from the TPP-EM correspond with the intersection of $Im[Z_{DBR}]$ and $-Im[Z_{CdO}]$. The dips in reflectivity of the DBR correspond with resonant features in $Im[Z_{DBR}]$. The large peaks in emissivity are a result of the high carrier density of the CdO film, and therefore the low $Re[Z_{CdO}]$ of the CdO within this spectral range. Above the plasma

frequency of the CdO, $Re[Z_{CdO}]$ increases substantially, thus, resulting in poor impedance matching between the DBR and the CdO. Fig. S17b displays the emissivity of two TPP-EMs with identical DBRs, but with one deposited on low-doped ($N_d = 7x10^{19}\ cm^{-3}$) and the other on high-doped ($N_d = 4.3x10^{20}\ cm^{-3}$) CdO films. Although for both carrier densities of CdO, $Im[Z_{DBR}]$ and $-Im[Z_{CdO}]$ intersect at similar frequencies (see **Fig. S19e**), the elevated $Re[Z_{CdO}]$ of the low carrier density TPP-EM film (see **Fig. S19f**) results in TPP modes not being supported above the plasma frequency of the CdO (dashed, vertical black line in **Fig. 19b**).

Section 20. The role of CdO in the inversely designed TPP-EMs: carrier concentration (real part of dielectric function) and mobility (imaginary part of dielectric function)

Here we extend the discussion of how the tunable dielectric function of CdO (both real part and imaginary part) leads to the enhanced spectral control. The dielectric function of CdO is mainly dictated by two components: carrier concentration ($\boldsymbol{N_d}$) and mobility. $\boldsymbol{N_d}$ mainly determines the real part while the mobility mainly decides the ratio of imaginary part over real part. In our paper, except for this section, the mobility is treated as a constant of 200 $cm^{-2}/V/s$ because our fabrication process does not change it dramatically. The $\boldsymbol{N_d}$ is designable as shown in experimental data.

The influence of carrier concentrations

As discussed in the main text regarding **Fig. 4a**, we observed that the CdO-based TPP-EM offers better performance, i.e., more close matching to the TS, yet the inverse design algorithm provides no physical intuition. Here we try to reveal the origin of how the tunable carrier concentration provides such substantial improvements to the performance of TPP-EMs. To this aim we run the same optimization to match the absorption spectrum of DMMP with different, fixed $\boldsymbol{N_d}$**s**, ranging from 0.2 to 120.0×10^{20} cm^{-3}, spaced exponentially, as shown in **Fig. S20a, b**. Note that the highest possible carrier concentration of CdO is 12.0×10^{20} cm^{-3}, according to the references[13,32], and we here extend to 120.0×10^{20} cm^{-3} purely to explore the mechanism. The number of dielectric layers in the DBR stack is fixed to 29 so that they are consistent with the main text **Fig. 4a**. We find that the performance of CdO-based TPP-EM is strongly defined by the carrier concentration: when the carrier concentration is below 1.0×10^{20} cm^{-3}, the optimized structures have similar performances. However, when the carrier concentration is fixed at a value above 4.0×10^{20} cm^{-3}, the performance degrades. Thus, we can consider the dielectric function of CdO (equivalently, the carrier concentration in our case) as a parameter, and our algorithm can optimize this value for a given task. From a physics perspective, the dielectric function of CdO (**Fig. S20c**) can be tuned via doping to adjust the impedance model (**Fig. S20d**) so that the spectra of TPP-EMs, which are determined by the impedance of the conducting layer and DBR together (**SI section 19**), can be matched to arbitrary spectra.

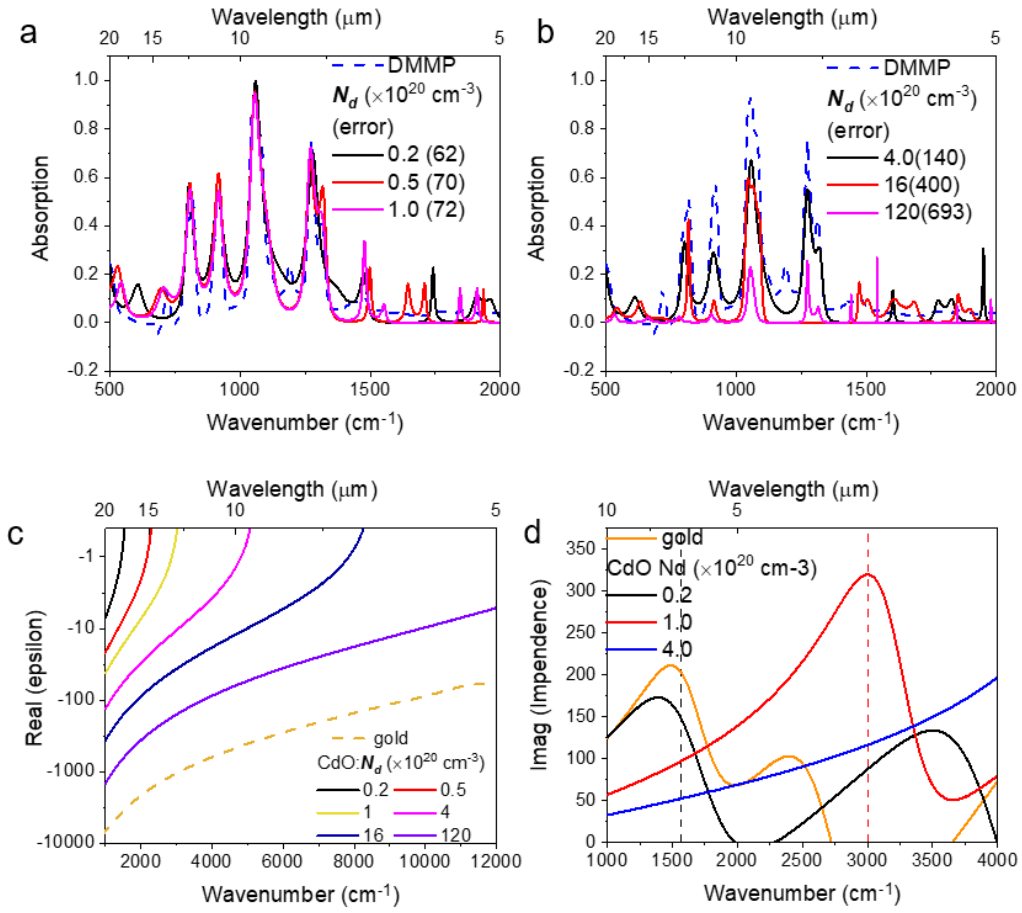

Fig. S20, Optimized TPP-EM when CdO carrier concentrations are fixed at different values. The errors are included in the parentheses.

The influence of mobilities

The CdO mobility determines the imaginary part of the dielectric function with a given carrier concentration (**Fig. S21b**), which should influence the performance of TPP-EM according to references [35-37]. Here we discuss what will happen if the mobility is increased (decreased) for improved fabrication techniques (restricted fabrication process for cost, compatibility issue, etc). We used the mobility of 200 $cm^{-2}/V/s$ for the calculations reported in the paper, which is roughly in line with the lower end of the observed values we measure experimentally for this material[13]. However, for this thought experiment, here we perform equivalent designs with artificially reduced and increased values of 50 and 800 $cm^{-2}/V/s$.

We first compare the highest accessible Q-factor with a given number of dielectric stacks (11 here) and find that higher Q-factors can be achieved with higher mobility films, i.e., lower imaginary part of CdO dielectric function, as expected (**Fig. S21a, b**). We then fixed the carrier concentration (N_d) of CdO and compared the performance of inversely designed TPP-EMs with different mobilities for the same tasks in Fig. S11b

and c with 11 and 29 dielectric layers, respectively. We find that the two tasks can be realized with the best performance at specific mobility values, which are both 50 $cm^{-2}/V/s$ for the task in **Fig. S21c, d**, respectively. Note that for the comparison we fixed the carrier concentration to 4.0×10^{20} cm^{-3}, however, at a different fixed carrier concentration the optimal mobility might become 200 or 800 $cm^{-2}/V/s$, as the mobility and carrier concentration together determine the complex dielectric function of CdO (thus optical properties). Finally, we fixed the mobility of CdO to 50, 200 and 800 $cm^{-2}/V/s$ and allowed the $\boldsymbol{N_d}$ to change freely. When the carrier density is allowed to vary to account for different mobility values, we observe comparable performances from all three even with dramatically different mobilities, as shown in **Fig. S21e, f**. Thus, the use of the CdO in which the carrier density can be controlled over a broad range implies that the increased/decreased mobility (loss of CdO) does not influence the performance of inversely designed TPP-EM for many tasks, providing such CdO-based designs unprecedented spectral control.

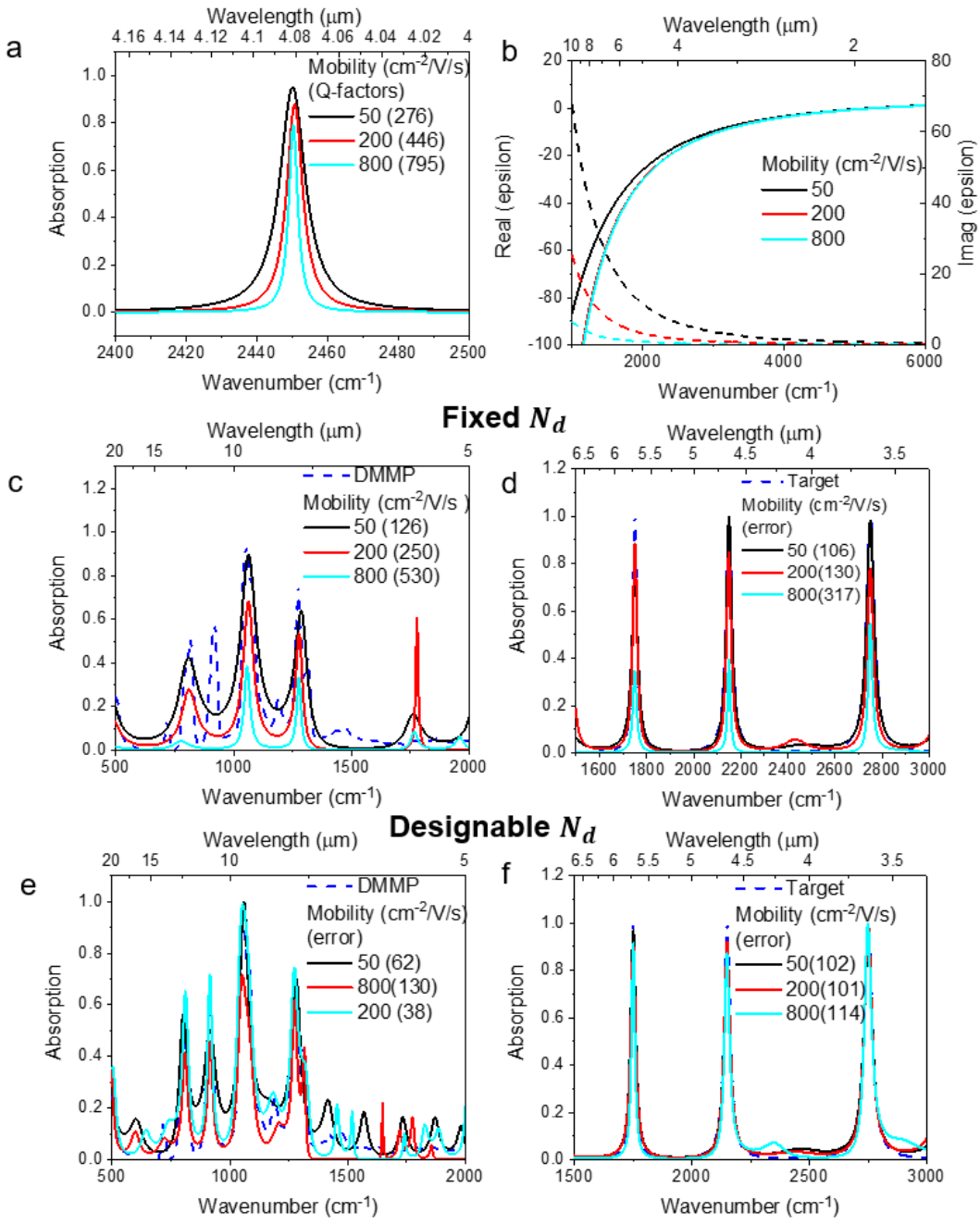

Fig. S21, Optimized TPP-EM with differently fixed mobilities. (a) Highest possible Q-factor with different mobilities; (b) dielectric function of CdO with different mobilities, while the N_d is 4×10^{20} cm^{-3}; (c, d) inversely designed TPP-EM with different mobilities while the N_d is fixed at 4×10^{20} cm^{-3}; (e, f) inversely designed TPP-EM with different mobilities while the N_d is designable. Errors or Q-factors are included in the parentheses.

References

1 Robbins, H. & Monro, S. A stochastic approximation method. *The annals of mathematical statistics*, 400-407, (1951).

2 Bordes, A., Bottou, L. & Gallinari, P. SGD-QN: Careful quasi-Newton stochastic gradient descent. *Journal of Machine Learning Research* **10**, 1737-1754, (2009).

3 Sohl-Dickstein, J., Poole, B. & Ganguli, S. Fast large-scale optimization by unifying stochastic gradient and quasi-Newton methods. 604-612.

4 Kingma, D. P. & Ba, J. Adam: A method for stochastic optimization. *arXiv preprint arXiv:1412.6980*, (2014).

5 Xiong, Y., Liu, Z. & Zhang, X. A simple design of flat hyperlens for lithography and imaging with half-pitch resolution down to 20 nm. *Applied Physics Letters* **94**, 203108, (2009).

6 https://my.vanderbilt.edu/caldwellgroup/.

7 Liang, W. *et al.* Ultranarrow-bandwidth planar hot electron photodetector based on coupled dual Tamm plasmons. *Optics Express* **28**, 31330-31344, (2020).

8 Sakurai, A. *et al.* Ultranarrow-band wavelength-selective thermal emission with aperiodic multilayered metamaterials designed by Bayesian optimization. *ACS central science* **5**, 319-326, (2019).

9 Botros, J., Ali, M. O., Tait, R. N., Amaya, R. E. & Gupta, S. Direct thermal emission testing of aperiodic dielectric stack for narrowband thermal emission at mid-IR. *Journal of Applied Physics* **127**, 114502, (2020).

10 Wang, Z. *et al.* Ultra-narrow and wavelength-tunable thermal emission in a hybrid metal-optical Tamm state structure. *ACS Photonics*, (2020).

11 Wang, Z., Ho, Y. L., Cao, T., Yatsui, T. & Delaunay, J. J. High‐Q and Tailorable Fano Resonances in a One‐Dimensional Metal‐Optical Tamm State Structure: From a Narrowband Perfect Absorber to a Narrowband Perfect Reflector. *Advanced Functional Materials*, 2102183, (2021).

12 So, S., Lee, D., Badloe, T. & Rho, J. Inverse design of ultra-narrowband selective thermal emitters designed by artificial neural networks. *Optical Materials Express* **11**, 1863-1873, (2021).

13 Nolen, J. R. *et al.* Ultraviolet to far-infrared dielectric function of n-doped cadmium oxide thin films. *Physical Review Materials* **4**, 025202, (2020).

14 Li, H. H. Refractive index of silicon and germanium and its wavelength and temperature derivatives. *Journal of Physical and Chemical Reference Data* **9**, 561-658, (1980).

15 Kagaya, H. M. & Soma, T. Temperature dependence of the linear thermal expansion coefficient for Si and Ge. *physica status solidi (b)* **129**, K5-K8, (1985).

16 De Silans, T. P. *et al.* Temperature dependence of the dielectric permittivity of CaF2, BaF2 and Al2O3: application to the prediction of a temperature-dependent van der Waals surface interaction exerted onto a neighbouring Cs (8P3/2) atom. *Journal of Physics: Condensed Matter* **21**, 255902, (2009).

17 Wang, T. *et al.* Phonon-polaritonic bowtie nanoantennas: controlling infrared thermal radiation at the nanoscale. *ACS Photonics* **4**, 1753-1760, (2017).

18 Caldwell, J. D. *et al.* Sub-diffractional volume-confined polaritons in the natural hyperbolic material hexagonal boron nitride. *Nature communications* **5**, 5221, (2014).

19 Caldwell, J. D. *et al.* Low-loss, extreme subdiffraction photon confinement via silicon carbide localized surface phonon polariton resonators. *Nano letters* **13**, 3690-3697, (2013).

20 Tamagnone, M. *et al.* High quality factor polariton resonators using van der Waals materials. *arXiv preprint arXiv:1905.02177*, (2019).
21 Autore, M. *et al.* Boron nitride nanoresonators for phonon-enhanced molecular vibrational spectroscopy at the strong coupling limit. *Light: Science &Amp; Applications* **7**, 17172, (2018).
22 Wang, B. *et al.* High‐Q Plasmonic Resonances: Fundamentals and Applications. *Advanced Optical Materials*, 2001520, (2021).
23 https://www.edmundoptics.com/f/infrared-ir-bandpass-filters/14290/.
24 Naganathappa, M., Waghmare, S. & Chaudhari, A. Infrared and electronic absorption spectra of formaldehyde in gas phase and astrophysical H 2 O ice. *Astrophysics and Space Science* **332**, 249-256, (2011).
25 Dong, M., Zheng, C., Miao, S., Song, F. & Wang, Y. A mid-infrared carbon monoxide sensor system using wideband absorption spectroscopy and a single-reflection spherical optical chamber. *Infrared Physics & Technology* **85**, 450-456, (2017).
26 Livingood, A. *et al.* Filterless Nondispersive Infrared Sensing using Narrowband Infrared Emitting Metamaterials. *ACS Photonics*.
27 Asano, T. *et al.* Near-infrared–to–visible highly selective thermal emitters based on an intrinsic semiconductor. *Science advances* **2**, e1600499, (2016).
28 Granier, C. H., Afzal, F. O., Min, C., Dowling, J. P. & Veronis, G. Optimized aperiodic highly directional narrowband infrared emitters. *JOSA B* **31**, 1316-1321, (2014).
29 Howes, A., Nolen, J. R., Caldwell, J. D. & Valentine, J. Near‐Unity and Narrowband Thermal Emissivity in Balanced Dielectric Metasurfaces. *Advanced Optical Materials* **8**, 1901470, (2020).
30 Liu, X. *et al.* Large-area, lithography-free, narrow-band and highly directional thermal emitter. *Nanoscale* **11**, 19742-19750, (2019).
31 Kaliteevski, M. *et al.* Tamm plasmon-polaritons: Possible electromagnetic states at the interface of a metal and a dielectric Bragg mirror. *Physical Review B* **76**, 165415, (2007).
32 Liu, C. P. *et al.* Effects of free carriers on the optical properties of doped CdO for full-spectrum photovoltaics. *Physical Review Applied* **6**, 064018, (2016).
33 Burnett, J. H., Kaplan, S. G., Stover, E. & Phenis, A. Refractive index measurements of Ge. **9974**, 99740X.
34 Gao, W. Spectroscopic ellipsometry studies on vacuum-evaporated zinc selenide thin film. **7283**, 72832L.
35 Brand, S., Kaliteevski, M. A. & Abram, R. A. Optical Tamm states above the bulk plasma frequency at a Bragg stack/metal interface. *Physical Review B* **79**, 085416, (2009).
36 Morozov, K. M. *et al.* Revising of the Purcell effect in periodic metal-dielectric structures: the role of absorption. *Scientific reports* **9**, 1-9, (2019).
37 Kaliteevski, M. A. *et al.* Experimental demonstration of reduced light absorption by intracavity metallic layers in Tamm plasmon-based microcavity. *Plasmonics* **10**, 281-284, (2015).